PHYSICAL REVIEW B VOLUME 23, NUMBER 10 15 MAY 1981

Fermi surface of lead under homogeneous strain

W. Joss
Laboratorium für Festkörperphysik, Eidgenössische Technische Hochschule, CH-8093 Zürich, Switzerland
(Received 25 July 1980)

The uniaxial stress and angular shear dependence of several extremal cross sections of the Fermi surface of the simple metal lead were obtained by a simultaneous measurement of the oscillatory magnetostriction and the de Haas–van Alphen torque. For six of the seven experimentally studied orbits all the uniaxial stress derivatives were determined and their sum compares well with the directly measured hydrostatic pressure dependence of other authors. The response of the Fermi surface to homogeneous strain is discussed in terms of volume-conserving shears (tetragonal or angular) and volume changes. A theoretical study of the Fermi surface and its strain dependence, based on a local pseudopotential model, is presented. New values for the relevant pseudopotential matrix elements in the absence of strain obtained from a fit to high-precision de Haas–van Alphen frequencies are given for different sizes [(4×4), (8×8), (16×16)] of the secular matrix. The Fermi energy and its derivatives are computed by summing over occupied states. Eight orthogonalized plane waves are required in the secular matrix in order to describe the effect of a general homogeneous deformation on the Fermi surface. The strain response of ten carefully extremalized orbits has been calculated, with the slopes of the form factor at the first two reciprocal-lattice vectors as the only free parameters. Good agreement with our uniaxial stress data, as well with the hydrostatic pressure data of Anderson *et al.* is found, without invoking the spin-orbit interaction as an extra free parameter.

I. INTRODUCTION

The precise experimental information obtainable from zero-pressure Fermi-surface studies stimulated the development of various theoretical models for the electronic band structure. For simple metals a plane-wave representation of the conduction-electron states in combination with a weakly scattering pseudopotential has been successful.[1,2] An experimental investigation of the effect of homogeneous strain on the Fermi surface provides a critical test of the physics involved in the description of the solid at *zero* pressure. The strain introduces additional degrees of freedom, namely, lattice and potential parameters entering the band-structure calculation must be allowed to vary with strain. In particular one may hope to gain further insight into the interaction between the conduction electrons and the lattice ions, which is responsible for the shape of the Fermi surface. If the model with strain-dependent parameters fails to account for the strain experiments, then the zero-strain model is highly questionable. Furthermore the study of the strain dependence of the Fermi surface is of great interest, because it provides information about the electronic energy band structure of solids under strain. Such information is invaluable for the understanding of the strain dependence of all properties in which the conduction electrons play an important role.

Of all simple metals, lead is the one for which the pressure dependence of the Fermi surface has been the most intensively studied. Anderson *et al.*[3] showed in their first investigation that the pressure dependence of the Fermi surface is strongly influenced by the stress dependence of the pseudopotential form factor. In a subsequent paper Anderson *et al.*[4] compared their experimental pressure derivatives to the predictions of various Fermi-surface models. They pointed out that although a local pseudopotential model including spin-orbit interaction accounts for the general topological features of the equilibrium Fermi surface of lead, it fails to correctly predict its pressure dependence. They had to assume a nonlocal and volume-dependent pseudopotential in order to reproduce their experimental results. Unfortunately, once the bare pseudopotential is allowed to vary with volume, the whole concept loses its physical significance, so that these author's results are not very meaningful. According to Van Dyke,[5] the 4-OPW (orthogonalized-plane-wave) calculation using a *local* pseudopotential failed to reproduce the correct pressure dependence because the number of plane waves considered was too small. Van Dyke obtained reasonably good agreement with the experimental values of Anderson *et al.*[4] with a local pseudopotential model involving 90 OPW's. On the other hand, a rough calculation by Sorbello and Griessen[6] based on a simple local 4-OPW model neglecting spin-orbit interaction, suggests that part of the difficulty encountered by the above authors in reproducing the experimental data is due to their expressing the matrix elements and Fermi energy in so-called computational units, i.e., factoring out a term inversely proportional to the lattice constant squared, whose dependence upon pressure was subsequently ignored. In order

to settle the question we undertook a careful experimental and theoretical investigation of lead.

Our results are given in such a way as to allow future workers to compute the response of the Fermi surface of lead to an arbitrary strain. The subsequent sections of the paper are arranged as follows: In Sec. II we introduce our notation for lattice deformation, discuss the experimental method, and describe the equipment. Finally we present the experimental results for various extremal cross sections of the Fermi surface of lead. The formalism for calculating the strain response is developed in Sec. III, which also contains our computational results and the comparison between the experimental and calculated values for the strain dependence of extremal cross sections. The conclusions are given in Sec. IV.

II. EXPERIMENTAL

A. Characterization of lattice strains and stresses

Here we recall the notions of elasticity necessary for the understanding of our discussion of the strain dependence of the Fermi surface. We restrict ourselves to the case of cubic crystals. The lattice strain is related to the applied stress through the elastic compliance constants S_{ij}.

Given three orthogonal unit vectors $\vec{x}, \vec{y}, \vec{z}$, attached to the unstrained lattice, a uniform deformation of the crystal will transform them into a new set of vectors $\vec{x}', \vec{y}', \vec{z}'$, of which $\vec{x}'$ is, for example, given by

$$\vec{x}' = (1+\epsilon_{xx})\vec{x} + \epsilon_{xy}\vec{y} + \epsilon_{xz}\vec{z} . \tag{2.1}$$

It will prove convenient to express the state of strain in terms of the associated dilation and six volume-conserving shears. The uniform dilation is given by

$$\Delta\Omega/\Omega = \epsilon_{xx} + \epsilon_{yy} + \epsilon_{zz} . \tag{2.2}$$

A volume-conserving *tetragonal* shear along the x axis is the following combination of the fractional strains ϵ_{ii}:

$$\epsilon_{xx} = \gamma_x ; \quad \epsilon_{yy} = \epsilon_{zz} = -\tfrac{1}{2}\gamma_x \tag{2.3}$$

and is defined by the symbol γ_x. A volume-conserving *angular* shear in the $x-y$ plane is given by

$$\gamma_{xy} = \gamma_{yx} = (\epsilon_{xy} + \epsilon_{yx}) . \tag{2.4}$$

Thus a positive angular shear γ_{ij} corresponds to a reduction in the angle between the i and j axes of the real-space lattice. The strain components above defined $\epsilon_{xx}, \epsilon_{yy}, \epsilon_{zz}, \gamma_{yz}, \gamma_{zx}, \gamma_{xy}$ are related to the stress components $\sigma_{xx}, \sigma_{yy}, \sigma_{zz}, \tau_{yz}, \tau_{zx}, \tau_{xy}$ by the matrix of elastic stiffness constants C_{ij}.

B. Measurement of the strain response

The response of the Fermi surface to uniaxial strain can be determined either directly by applying an external stress to the sample or indirectly from oscillatory magnetostriction or sound-velocity measurements. The first kind of experiments bring with them the risk of damaging or rotating the sample when applying the stress, while the sound-velocity measurements only produce products of strain derivatives, so that the second of the three methods appears to be the most reliable.[7] The uniaxial stress dependence of a Fermi-surface cross section can be measured by combining the amplitude of the oscillatory magnetostriction and the de Haas–van Alphen torque as discussed in detail by Griessen and Sorbello.[8] Advantage is taken of the oscillatory behavior of the thermodynamic potential[9] of an electron gas in an external magnetic field H as a function of the inverse of the latter. For an oscillatory strain $\epsilon_{ii}(H)$ measured parallel to the crystallographic axis i, the corresponding stress dependence of an extremal orbit of area A is given by the relation

$$\frac{d\ln A}{d\sigma_{ii}} = -\frac{\epsilon_{ii}(H)}{\tau(H)} \frac{d\ln A}{d\phi} , \tag{2.5}$$

where τ is the de Haas–van Alphen torque per unit volume measured with an arbitrarily chosen suspension axis. The angle ϕ is measured in a plane perpendicular to the suspension axis and specifies the orientation of the sample with respect to the magnetic field. The amplitudes of the oscillatory quantities are measured at the same temperature, orientation, and magnetic field strength, and the relative phase between ϵ_{ii} and τ determines the sign of the stress dependence. τ and the $d\ln A/d\phi$ often vanish for a field applied along a symmetry axis whereas the quotient $\tau/(d\ln A/d\phi)$ can be accurately extrapolated from measurements of the two quantities as a function of the magnetic field orientation. The main limitation of the method arises from *torque-induced* length changes, in particular in those cases where the *magnetostrictive* length changes are small to begin with. These spurious effects are easily detected by measuring the amplitude of the oscillatory magnetostriction as a function of ϕ in the neighborhood of symmetry planes or axis. If $A(\phi)$ has an extremum in the chosen symmetry direction, then the relative length change must be a symmetric function of ϕ about that direction. Any deviation from symmetry can be attributed to tor-

que effects.

The oscillatory relative length changes of the sample dimension $\Delta l/l$ in an arbitrary crystallographic direction $\vec{e}$ (unit vector) is given by

$$\frac{\Delta l}{l} = \sum_i^3 \left(\sum_j^3 \epsilon_{ij} e_j \right) e_i . \tag{2.6}$$

Equation (2.5) is also valid for off-diagonal elements ϵ_{ij} [defined in Eq. (2.1)], and combining it with Eq. (2.6) we obtain

$$\sum_{i,j}^3 e_i e_j \frac{d \ln A}{d\sigma_{ij}} = -\frac{\Delta l/l}{\tau} \frac{d \ln A}{d\phi} . \tag{2.7}$$

For length changes measured in the [110] direction the left-hand side of Eq. (2.7) becomes

$$\frac{1}{2}\left(\frac{d \ln A}{d\sigma_{xx}} + \frac{d \ln A}{d\sigma_{yy}} + \frac{d \ln A}{d\tau_{xy}} \right), \tag{2.8}$$

where use has been made of the identity

$$\frac{d \ln A}{d\tau_{xy}} = \frac{d \ln A}{d\sigma_{xy}} + \frac{d \ln A}{d\sigma_{yx}} . \tag{2.9}$$

Similarly for $\vec{e}$ parallel to the [111] direction we get

$$\frac{1}{3}\left(-\frac{d \ln A}{dp} + \frac{d \ln A}{d\tau_{yz}} + \frac{d \ln A}{d\tau_{zx}} + \frac{d \ln A}{d\tau_{xy}} \right). \tag{2.10}$$

It is therefore apparent that the method also gives access to the angular shear dependence of extremal orbits. The first term in Eq. (2.10) was obtained from the relation

$$\frac{d \ln A}{dp} = -\sum_i^3 \frac{d \ln A}{d\sigma_{ii}} . \tag{2.11}$$

The pressure derivative can in turn be related to the volume derivative by

$$\frac{d \ln A}{dp} = -\kappa \frac{d \ln A}{d \ln \Omega} = -\frac{\kappa}{3} \sum_i^3 \frac{d \ln A}{d\epsilon_{ii}} , \tag{2.12}$$

where κ, the isothermal compressibility, is equal to $3(S_{11}+2S_{12})$ for the cubic metals considered. The tetragonal shear derivatives are obtained from the measured stress derivatives by means of the relationship

$$\frac{d \ln A}{d\gamma_i} = (C_{11}-C_{12})\left[\frac{d \ln A}{d\sigma_{ii}} - \frac{1}{2}\left(\frac{d \ln A}{d\sigma_{jj}} + \frac{d \ln A}{d\sigma_{kk}} \right) \right], \tag{2.13}$$

which follows from the definition of the tetragonal shear dependence

$$\frac{d \ln A}{d\gamma_i} = \frac{d \ln A}{d\epsilon_{ii}} - \frac{1}{2}\left(\frac{d \ln A}{d\epsilon_{jj}} + \frac{d \ln A}{d\epsilon_{kk}} \right). \tag{2.14}$$

In terms of the response of the Fermi surface to a uniform dilation and a volume-conserving shear, the effect of a uniaxial strain on the extremal area A is given by

$$\frac{d \ln A}{d\epsilon_{ii}} = \frac{2}{3} \frac{d \ln A}{d\gamma_i} + \frac{d \ln A}{d \ln \Omega} , \tag{2.15}$$

which follows from Eqs. (2.12) and (2.14). The dependence of an extremal area upon stress can be obtained from Eq. (2.15) with help of the identity

$$\sum_{i=1}^3 \frac{d \ln A}{d\gamma_i} = 0 \tag{2.16}$$

and using the definition of the elastic compliance constant S_{ij}. The result is

$$\frac{d \ln A}{d\sigma_{ii}} = \tfrac{2}{3}(S_{11}-S_{12}) \frac{d \ln A}{d\gamma_i} + \frac{\kappa}{3} \frac{d \ln A}{d \ln \Omega} . \tag{2.17}$$

C. Experimental equipment

Two different sample holders were used to measure *simultaneously* the oscillatory magnetostriction and the de Haas–van Alphen torque by means of a capacitance technique. The dilatorquemeter I shown in Fig. 1 contains a dilatometer with an adjustable capacitor gap. The gap can be externally set at any temperature, which guarantees excellent sensitivity of the device irrespective of

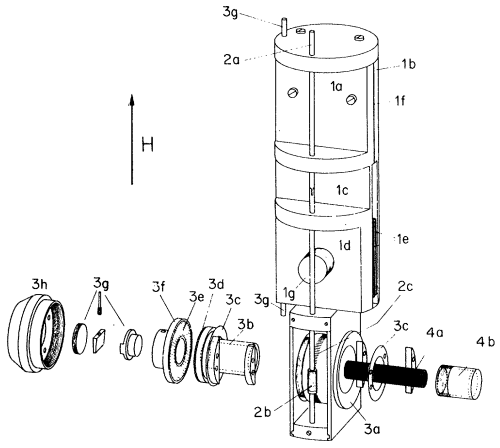

FIG. 1. Schematic view of the dilatorquemeter. 1- torquemeter with 1*a* - and 1*b*- fixed parts, 1*c*- thin part acting as spring, 1*d*- moveable part, 1*e*- rectangular capacitor plates, 1*f*- spacer, 1*g*- calibrated feedback coil. 2- worm drive with 2*a*- rotation shaft, 2*b*- worm, 2*c*- worm wheel. 3- dilatometer with 3*a* - fixed part, 3*b*- moveable part, 3*c*- ring spring system for a parallel displacement of part 3*d*- ring capacitor plate, 3*e*- fixed ring capacitor, 3*f*- capacitor plate holder with guard rings, 3*g*- gap adjustment system consisting of a moveable wedge-shaped part, 3*h*- screw cap, 4*a*- sample, 4*b*- mounting cap screwed on 3*b*. The dilatorquemeter fits into a bore of about 4 cm in diameter.

the thermal expansion of the measured material. The dilatometer 3, with the sample 4*a* inside is mounted on the torquemeter 1 and can be rotated about an axis perpendicular to the field by means of the rod 2*a* and the worm drive 2*b* and 2*c*. The moveable end of the torquemeter 1*d* is connected to the fixed end 1*a* by a thin tongue 1*c* (1 mm thick) acting as a spring, and the whole piece is machined out of a single block of material, with great care taken to eliminate possible internal tensions. The rectangular capacitor plates 1*e* are isolated and glued on the parts 1*b* and 1*d* and lapped together with the planes containing the spacer 1*f* (typically 0.05 mm thick). To prevent some previously observed interactions between the dilatometer and the torquemeter, the latter's compliance was improved by an electronic feedback system. This system sends a compensating current through the coil 1*g*, thereby compensating the de Haas–van Alphen torque with the torque resulting from the action of the magnetic field on the magnetic moment of this coil. This feedback system now yields a sensitivity of 10^{-8} N m with a torquemeter compliance of only 10^{-3} rad/N m. Following Brändli and Griessen,[10] we fixed the moveable part of the dilatometer 3*b* with two ring springs 3*c* onto the hollow cylindrical body 3*a*, which produced a parallel displacement of the capacitor plate 3*d*. One end of the sample 4*a* fits into the mounting cap 4*b*, screwed on the moveable part 3*b*. The other end pushes the plunger of the gap adjustment system 3*g*. The plunger can be moved with a wedge and a screw mounted in the capacitor plate holder 3*f*. The gap will be adjusted in the beginning of the experiment at liquid-helium temperature and afterwards the turning rod 3*g* will be disconnected. Best possible parallelism of the two capacitor plates was achieved by lapping simultaneously the capacitor plate 3*d* and the left rim of the body 3*a*. During the lapping the spring system was loaded so that in the equilibrium position the capacitor plate 3*d* and the rim of 3*a* are separated by a distance of 1 mm along the axis. The capacitor plate 3*e* and the guard ring 3*f* were also lapped together. After screwing the cap 3*h* onto 3*a*, the capacitor plate holder 3*f* was pushed with screws against the rim of 3*a*. In this way a very good parallelism of the capacitor plates could be achieved, so that small gaps of the order of 0.01 mm could be used for the measurements and the resulting sensitivity was 5×10^{-11} for relative length changes.

The sample holder I allows measurements only of the response of extremal areas to a stress perpendicular to the applied magnetic field. For measurements of the oscillatory magnetostriction in an arbitrary direction with respect to the magnetic field, a second dilatorquemeter (II) similar to the one described by Griessen *et al.*[11] was constructed. The torque is again electronically compensated by a feedback system and gives us a sensitivity of 10^{-9} N m with a torque compliance of only 10^{-2} rad/N m. The sample is glued on a conical polycrystalline support of the same material as the sample. The upper face of the sample acts as one of the capacitor plates of the dilatometer. For samples with bigger thermal expansion than the material of the dilatometer (i.e., lead), the capacitor gap cannot be adjusted, and is given by the difference in the thermal expansion of the two materials. To avoid any magnetic effects all the parts including screws of the two dilatorquemeters were machined from the beryllium-copper alloy[12] which also has excellent mechanical properties. The dilatorquemeters were mounted on an evacuable vessel filled with helium exchange gas for thermal contact. Any traces of solid air would hinder the free movements of the rotatable parts.

The oscillatory magnetostriction and the de Haas–van Alphen torque were measured through a minicomputer-based data-acquisition system at temperature between 4.2 and 1.3 K in magnetic fields up to 10.5 T provided by a superconducting solenoid with a homogeneity of 1×10^{-6} over a volume of 1 cm^3. The homogeneity was adjusted by two compensating coils and checked over the whole field range by moving a pickup coil with constant velocity along the solenoid axis. The field was once calibrated with NMR and periodically checked with the help of the de Haas–van Alphen effect. Our measurement technique gives accurate values for the amplitude of both effects, but on the other hand, it does not permit any direct frequency discrimination, in contrast to the field modulation technique. To recover small de Haas–van Alphen frequency components which were buried in the side lobes of the Fourier spectrum of much larger components, our data were filtered using an equal-ripple finite-impulse-response digital filter.[13] The first points of the filtered output corresponding to the length of the impulse response were discarded (typically 41 of the 256 or 81 of the 512 data points). The cutoff frequency was chosen as far as possible from the de Haas–van Alphen frequencies of interest. The stress dependence is unaffected by small errors in the amplitudes of the magnetostriction and the torque caused by the filter. Both signals are affected in the same way, and to determine the stress dependence one uses the quotient of the two amplitudes. Closely-lying interfering frequencies were separated by a nonlinear fitting technique.[14]

D. Experimental results

The Fermi surface of lead has been investigated in detail by Anderson and Gold[15] using an impulsive-field de Haas–van Alphen technique. Their results are in qualitative agreement with an empty-lattice second- and third-zone Fermi surface based on four conduction electrons per atom. The large closed second-zone hole surface schematically shown in Fig. 2 as well as the multiply connected third-zone electron surface of [110] arms shown in Fig. 3 should have smaller dimensions than those predicted by the empty-lattice model. The latter also predicts small electron pockets in the fourth zone, centered at the zone corners W. These pockets, which have never been observed with the de Haas–van Alphen effects but whose existence had already been suggested by Tobin *et al.*'s[16] Shubnikov–de Haas experiment, have recently been confirmed by Ivowi and Mackinnon[17] in their study of quantum oscillations in ultrasonic absorption.

In Table I we present quantum oscillation frequencies obtained by different methods in high-symmetry directions. The listed de Haas–van Alphen data are the most accurate ones available to date. Our own results were obtained from simultaneous measurements of the oscillatory magnetostriction and de Haas–van Alphen torque. In all cases the observed frequencies of the two effects were identical. Except for the $\xi[100]$ and $\psi[111]$ orbits our values are in perfect agreement with the field modulation de Haas–van Alphen results. For $\zeta[110]$ we see the by-now well established 42.5-cycle beat pattern. For $\xi[100]$ and $\psi[111]$, which are both minimal, our results are probably the more reliable ones since (i) they were measured *simultaneously* with $\nu[100]$ or $\theta[111]$, for which no discrepancy was observed, and (ii) their angular dependence is weak which excludes errors from misalignment.

As for the samples used in our work, they were 99.9999% pure lead single crystals obtained from Metals Research or home grown from the melt in vacuum by the Czochralski technique. Unless the crystals were carefully annealed, mounted, and cooled, a spurious splitting of the ζ and ν branches was observed. The resulting beat patterns in the oscillatory magnetostriction and in the de Haas–van Alphen torque were strongly dependent on the orientation of the magnetic field, and in no way correlated. In contrast to this behavior our final samples displayed only two ζ frequencies in agreement with the results of Anderson *et al.*[19] For the ν orbit the splitting, although strongly reduced, could not be totally eliminated even in the best samples. Our conclusion is that

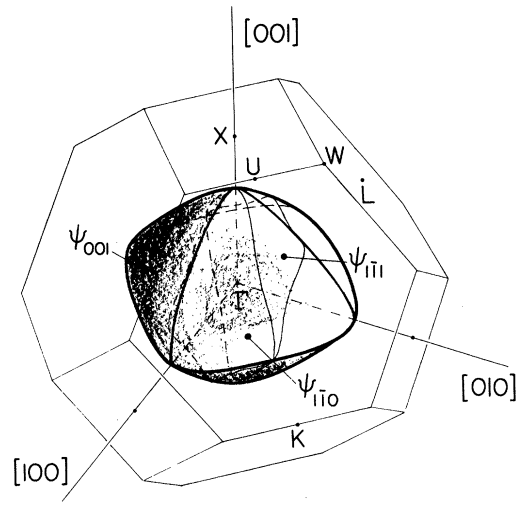

FIG. 2. Second-zone hole sheet of the Fermi surface of lead. The orbit ψ is drawn for the magnetic fields in the [001], [1$\bar{1}$0], and [1$\bar{1}$1] direction.

it cannot be ascribed to the interference of two adjacent frequencies, as suggested by Gold and Schmor[20] and others. A possible interpretation is that the effect is caused by the presence of small microcrystallites,[19] the number of which increases with each cooling cycle.[21]

The crystals measured in dilatorquemeter I were cylinders ($\phi 6 \times 20$ mm) with axes in the [100] and [110] direction. The orientation was accurate to within 2°. The oscillatory magnetostrictive length change $\Delta l/l$ was recorded along the cylinder axis. The torque τ was measured about the same direction, which is also the axis

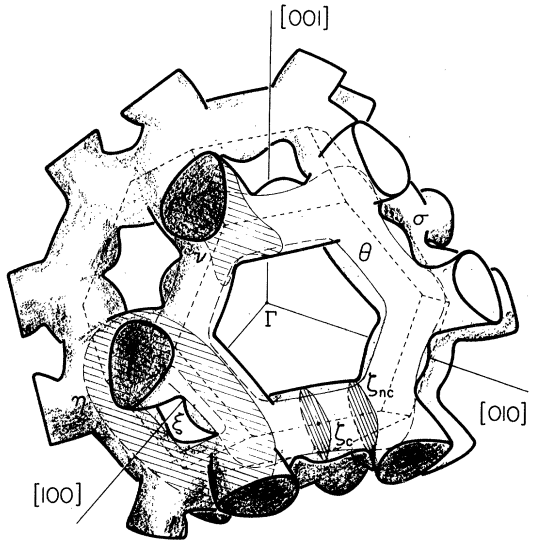

FIG. 3. Third-zone electron sheet of the Fermi surface of lead. The orbits ν, ξ, and η are drawn for the magnetic field in the [100] direction, ζ in the [1$\bar{1}$0] direction, and θ and σ in the [111] direction.

TABLE I. Quantum oscillation frequencies in lead. dHvA: de Haas–van Alphen effect. UQO: Ultrasonic quantum oscillations, Ref. 17. SdH: Shubnikov–de Haas effect, Ref. 16.

Orbit $[\vec{H}]$	Zone	Frequency (T) This work	dHvA	UQO	SdH
l[100]	4			565	
l[110]	4			440 ± 10	440 ± 20
l[111]	4			445	
l[112]	4				300 ± 20
ζ_c[110]	3	1 806 ± 2	1 807.2 ± 0.4[c]	1 833	1820 ± 10
ζ_{nc}[110]	3	1 764 ± 2	1 764 ± 6[cd]	1 795	
ζ[111]	3		2 237 ± 0.05[bd]	2 220	
ν[100]	3	5 126 ± 2	5 124.5 ± 0.2[ac]	5 010	
ω[110]	3			4 000 ± 200	
ξ[100]	3	3 564 ± 2	3 604 ± 20[b]	3 520	
θ[111]	3	10 921 ± 10	10 950 ± 30[b]	11 000	
ψ[100]	2	20 440 ± 10	20 436 ± 2[a]		
ψ[110]	2	15 917 ± 10	15 912 ± 5[abc]		
ψ[111]	2	15 472 ± 10	15 580 ± 40[b]		

[a] Reference 18.
[b] Reference 4.
[c] Reference 19.
[d] Error bars, J. R. Anderson, private communication.

about which the dilatometer can be rotated. This experiment only yields the response of extremal areas to a stress perpendicular to the applied magnetic field. These results were completed by extended measurements on a crystal ($\phi 5 \times 4$ mm) with [001] orientation. $\Delta l/l$ was measured along the [001] direction of the crystal lattice. The torque was measured about the [010] as well as about the [1$\bar{1}$0] direction, which is in this case the axis about which the dilatorquemeter can be rotated. The amplitude of the relative length changes as a function of magnetic field orientation is shown in Fig. 4 for all observed orbits. The quoted values correspond to averages over a certain range of magnetic field strength (ζ: 6.4–10.3 T; ν, ξ: 7.3–8.0 T; θ, ψ: 9.1–10.3 T) so as to optimize the signal. The angular dependence $d \ln A/d\phi$ was determined from the measured de Haas–van Alphen frequency with a typical accuracy of 2%. The quantity $\tau/(d \ln A/d\phi)$ occurring in the expression for the stress dependence, and which for our experimental configurations is the product of magnetization and magnetic field, is displayed in Fig. 5 for the same ranges of magnetic field strength. For a given orbit the amplitudes in Figs. 4 and 5 show a similar angular dependence. The torque amplitudes have cubic, the length changes tetragonal, symmetry, and the stress dependence $d \ln A/d\sigma_{001}$ calculated with Eq. (2.5) from the two quantities is shown in Fig. 6. Except for the second-zone ψ areas, which are on a large sheet of the Fermi surface which deforms

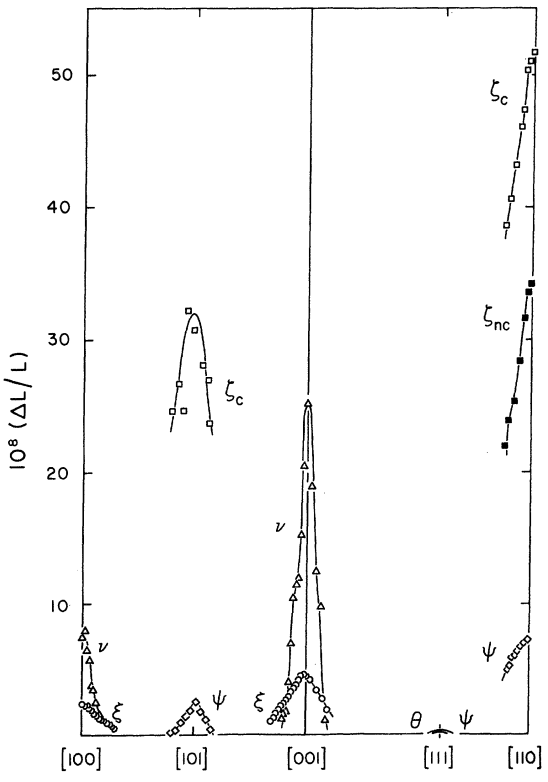

FIG. 4. Amplitude of magnetostrictive oscillations in the [001] direction at 1.4 K as a function of magnetic field orientation. The values quoted are averages over optimum ranges of magnetic field intensity (see text).

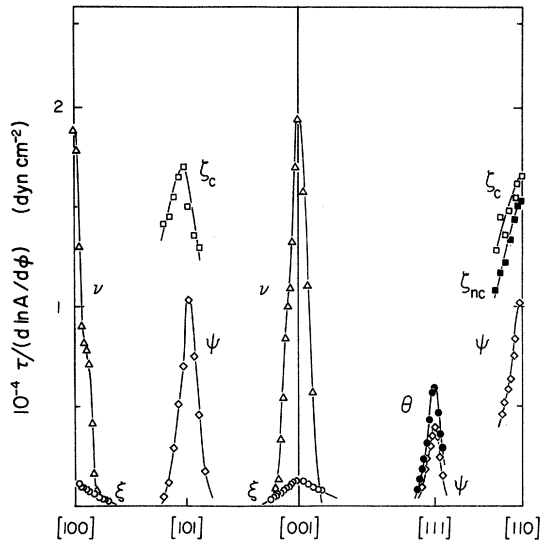

FIG. 5. de Haas–van Alphen torque normalized to relative change in area with field orientation as a function of the latter. Data obtained at 1.4 K and for different field ranges (see text).

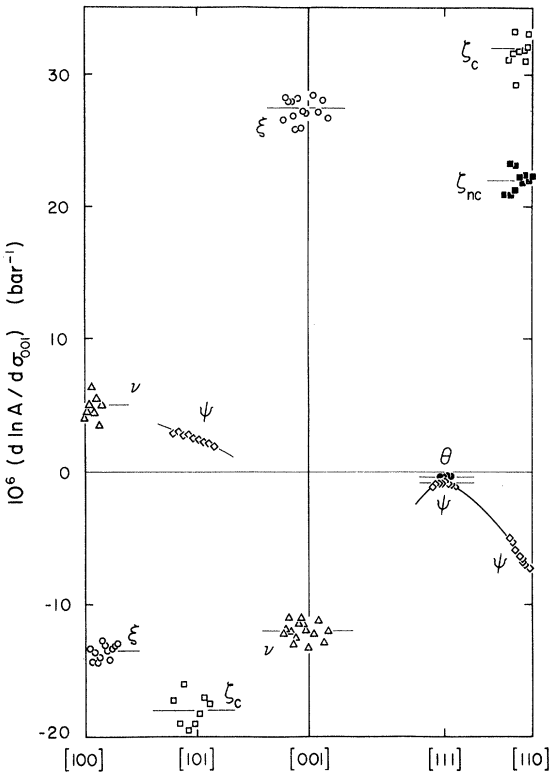

FIG. 6. Uniaxial stress dependence of extremal cross sections of the Fermi surface of lead as a function of field orientation, for magnetic fields in the (010) and $(1\bar{1}0)$ planes.

anisotropically under uniaxial stress, the stress dependences of the smaller orbits are only weakly dependent on the field orientation.

The stress dependences in high-symmetry directions are summarized in Table II. The values quoted are averages over several measurements

TABLE II. Experimental stress and hydrostatic pressure derivatives of extremal cross-sectional areas of the Fermi surface of lead.

Orbit $[\vec{H}]$	A (a.u.)	σ_{hkl}	$\frac{d\ln A}{d\sigma_{hkl}}$ (10^{-6} bar^{-1})	$\frac{d\ln A}{dp}$ (10^{-6} bar^{-1}) a	b
ζ_c[110]	0.0483	$\sigma_{100}, \sigma_{010}$	−18 ±4	4.0 ± 7	2.5 ± 0.2
		σ_{001}	32 ±4		
ζ_{nc}[110]	0.0472	σ_{001}	22 ±4		
ξ[111]	0.0598				2.7 ± 0.2
ν[100]	0.1370	σ_{100}	−12 ±2	2.0 ± 2.3	2.3 ± 0.1
		$\sigma_{010}, \sigma_{001}$	5 ±1		
ξ[100]	0.0953	σ_{100}	27.5 ± 2	−0.5 ± 2.3	0.0 ± 0.3
		$\sigma_{010}, \sigma_{001}$	−13.5 ± 1		
θ[111]	0.2919	$\sigma_{100}, \sigma_{010}, \sigma_{001}$	−0.4 ± 0.1	1.2 ± 0.2	1.2 ± 0.1
ψ[100]	0.5464				2.4 ± 0.4
ψ[110]	0.4255	$\sigma_{100}, \sigma_{010}$	2.4 ± 0.2	2.3 ± 0.5	2.9 ± 0.2
		σ_{001}	−7.1 ± 0.4		
ψ[111]	0.4136	$\sigma_{100}, \sigma_{010}, \sigma_{001}$	−0.8 ± 0.1	2.4 ± 0.2	2.1 ± 0.2
ζ_c[1$\bar{1}$0]	0.0483	σ_{110}	−16 ±4		
ν[001]	0.1370	σ_{110}	6 ±1		
ξ[001]	0.0953	σ_{110}	−13 ±1		
ψ[1$\bar{1}$0]	0.4255	σ_{110}	−1.7 ± 0.3		

[a] From uniaxial stress data (this work and Ref. 22).

[b] Direct measurements by Anderson *et al.* (Ref. 4).

in different experimental configurations. Table II also contains the result from the measurement on the crystal with its axis in the [110] direction. This geometry provides us with a nice consistency check, since the two uniaxial stress dependences appearing in the expression (2.8) are identical for the orbits under consideration and furthermore, the angular shear dependence of the $\nu[001]$ and $\xi[001]$ areas vanishes. This has the consequence that for the latter two orbits the following identity has to be satisfied:

$$\frac{d\ln A}{d\sigma_{110}} = \frac{d\ln A}{d\sigma_{xx}} = \frac{d\ln A}{d\sigma_{yy}}\,, \tag{2.18}$$

which is indeed the case. Finally, according to Eq. (2.11) the sum of our uniaxial stress dependences should be equal to the measured hydrostatic pressure derivatives. For all orbits this relation is satisfied within error bars, which is really significant only in the case of the $\theta[111]$, $\psi[110]$, $\psi[111]$ orbits for which the errors in the pressure derivatives calculated from the uniaxial stress data are small.

III. THEORETICAL

A. Formalism

In the pseudopotential approach, the secular matrix at the Fermi energy E_F is given in atomic units by

$$\vec{M}(\epsilon) = (\{\tfrac{1}{2}[\vec{k} - \vec{G}_i(\epsilon)]^2 - E_F(\epsilon)\}\delta_{\vec{G}_i\vec{G}_j} + V_{\vec{G}_i\vec{G}_j}(\epsilon))\,. \tag{3.1}$$

The $\vec{G}_i$'s are reciprocal-lattice vectors, ϵ stands for the lattice strain, and $V_{\vec{G}_i\vec{G}_j}$ are pseudopotential matrix elements conveniently expressed as

$$V_{\vec{G}_i\vec{G}_j} = S(\vec{G}_i - \vec{G}_j)\langle \vec{k} - \vec{G}_i | v | \vec{k} - \vec{G}_j\rangle\,, \tag{3.2}$$

where the structure factor $S(\vec{G}_i - \vec{G}_j)$ depends only on the geometry, and the form factor $\langle \vec{k} - \vec{G}_i | v | \vec{k} - \vec{G}_j\rangle$ is a property of the individual ion, independent of its lattice position. Since one is interested only in the first few eigenvalues λ of the infinite secular matrix, $\vec{M}$ is folded down to a finite size and the matrix elements are approximated by $V_{\vec{G}_i\vec{G}_j} = S(\vec{G}_i - \vec{G}_j)v(|\vec{G}_i - \vec{G}_j|)$, the so-called "on-Fermi-sphere" approximation.[2]

The Fermi surface of a homogeneously strained crystal is given by the locus of wave vectors $\vec{k}$ which satisfy the implicit equation

$$\lambda(\vec{k}, E_F(\epsilon), V_{\vec{G}_i\vec{G}_j}(\epsilon), \epsilon) = 0\,. \tag{3.3}$$

The strain dependence of a given orbit on the Fermi surface can, in principle, be obtained from two separate solutions of Eq. (3.3), one for the strained and one for the unstrained lattice. It is, however, more accurate to calculate directly the strain derivatives of the wave vector at each point of the orbit for $\epsilon = 0$.[11] This is done by differentiating the secular matrix $\vec{M}$ with respect to $x = \epsilon$, E_F and $V_s = S(\vec{G}_s)v(|\vec{G}_s|)$ analytically, and using the Hellman-Feynman theorem[23,24] to compute the derivatives of the eigenvalues

$$\frac{\partial\lambda}{\partial x} = \left\langle \Psi_0 \middle| \frac{\partial\vec{M}}{\partial x} \middle| \Psi_0 \right\rangle. \tag{3.4}$$

Here $|\Psi_0\rangle$ is the eigenvector corresponding to the eigenvalue at zero deformation. In order to remain on the $\lambda(\vec{k}, x) = 0$ surface as the parameter x varies, one imposes the condition that the *total* derivative $d\lambda/dx$ must vanish, i.e.,

$$\nabla_{\vec{k}}\lambda \cdot \frac{d\vec{k}}{dx} + \frac{\partial\lambda}{\partial x} = 0\,. \tag{3.5}$$

The dependence of the cross-sectional area of an orbit on the parameter x is determined by the component normal to the line element ds, of the projection of $d\vec{k}/dx$ in the plane of the orbit:

$$\frac{\partial A}{\partial x} = \oint_{\text{orbit}} \frac{d\vec{k}}{dx} \cdot \frac{(\nabla_{\vec{k}}\lambda)_\perp}{|(\nabla_{\vec{k}}\lambda)_\perp|}\, ds\,, \tag{3.6}$$

where $(\nabla_{\vec{k}}\lambda)_\perp$ is the component of the gradient perpendicular to the magnetic field. For extremal orbits the perpendicular component can be replaced by the full gradient in the numerator, since the parallel components obey the extremality condition

$$\oint_{\text{orbit}} \frac{|(\nabla_{\vec{k}}\lambda)_\parallel|}{|(\nabla_{\vec{k}}\lambda)_\perp|}\, ds = 0 \tag{3.7}$$

and $(d\vec{k}/dx)_\parallel$, the variation of $\vec{k}$ parallel to the field, is constant over the orbit if the latter is to remain in a plane perpendicular to the field. With help of Eq. (3.5) we finally find

$$\frac{\partial A}{\partial x} = -\oint_{\text{orbit}} \frac{\partial\lambda/\partial x}{|(\nabla_{\vec{k}}\lambda)_\perp|}\, ds\,. \tag{3.8}$$

To avoid uncertainties in the calculation of the line integral, it is convenient to express Eq. (3.8) in polar coordinates[11,24]

$$\frac{\partial A}{\partial x} = -\int_0^{2\pi} \frac{k_\perp^2(\partial\lambda/\partial x)}{(\vec{k}_\perp \cdot \nabla_{\vec{k}}\lambda)}\, d\phi\,, \tag{3.9}$$

where $\vec{k}_\perp = \vec{k}_\perp(\phi)$ is the radius vector for a point on the orbit and ϕ is the azimuthal angle. The response of an extremal cross-sectional area to a general strain ϵ is given by the following total derivative:

$$\frac{d\ln A}{d\epsilon} = \frac{\partial \ln A}{\partial \epsilon} + \sum_s \frac{\partial \ln A}{\partial \ln V_s} \frac{d\ln V_s}{d\epsilon}$$

$$+ \frac{\partial \ln A}{\partial \ln E_F} \frac{d\ln E_F}{d\ln\Omega} \frac{d\ln\Omega}{d\epsilon}, \qquad (3.10)$$

where all partial derivatives of A can be calculated by means of Eq. (3.8) or (3.9). [In the empty lattice case, the partial derivatives with respect to the strain ϵ and the Fermi energy E_F obtained from Eq. (3.9) were found to be identical to within 0.01% with the exact analytical result.]

B. The unstrained Fermi surface

For the calculation of the Fermi surface we use a secular matrix with a fixed number of plane waves (4, 8, or 16 OPW, the corresponding reciprocal-lattice vectors are given in Ref. 25). This is one possible choice of basis among many, none of them being entirely satisfactory in all respects. The fixed size of the matrix avoids discontinuities on the Fermi surface in the irreducible part of the Brillouin zone. Our choice of reciprocal-lattice vectors achieves complete equivalence between points on the Brillouin-zone surface which have the same symmetry, e.g., $U(1, \frac{1}{4}, \frac{1}{4})$ and $K(\frac{3}{4}, \frac{3}{4}, 0)$, but has the disadvantage that possibly not all members of a degenerate set of plane waves are included in the secular equation. This can lead to unphysical cusps in the band structure when the k vector crosses a high-symmetry axis, and to serious errors in computed properties which depend critically on the symmetry of the wave functions. More precisely, these effects are due to the asymmetric treatment of matrix elements connecting high-energy bands to those crossing the Fermi level. The mixing of these high-energy states into the ones on the Fermi surface is determined by the ratio of the matrix element squared, divided by the difference in kinetic energies, which is quite large for lead.[26] To reduce this asymmetry we set the higher ($|\vec{G}_i - \vec{G}_j| > 2k_F$) matrix elements equal to zero. We also neglect the spin-orbit interaction, which is important at the point W about 0.04 a.u. below the Fermi energy, where it opens a gap between the second and third band, but does not dramatically effect the general topology of the Fermi surface.

Our zero-temperature lattice constant differs by 0.3% from the one quoted by Anderson and Gold,[15] Anderson *et al.*,[4] and Van Dyke,[5] due to the use by the first authors of too high a value for the thermal expansion coefficient. Our value can be found in Table III together with other equilibrium parameters for Pb at 0 K. The coefficients $v_{111} = v(|\vec{G}_{111}|)$, $v_{200} = v(|\vec{G}_{200}|)$, and the Fermi energy E_F are treated as parameters in our calculation and their optimum values are listed in Table IV for three different sizes of the secular matrix. They result from unweighted least-squares fits to the area of eight extremal orbits on the unstrained second- and third-zone surface. The fits involved the derivatives of the areas with respect to the parameters and for different initial conditions always the same minimum was reached. The coefficient v_{111} is relatively constant as a function of the size of the secular matrix and v_{200} tends towards the value of the form factor at $q = |\vec{G}_{200}|$ given by Appapillai and Williams.[26] We note that our 8-OPW coefficients v_{111} and v_{200} are very similar to those of the local 4-OPW calculation with spin-orbit of Anderson *et al.*[4] ($v_{111} = -0.047, v_{200} = -0.0285$ a.u.) and that Van Dyke,[5] using about 90 OPW's, found about the same value for v_{111} ($= -0.0511$ a.u.) but a much bigger coefficient $v_{200}(= -0.0105$ a.u.). We redetermine the Fermi energy by summing over occupied states with the Gilat-Raubenheimer method.[31] In all cases the metal is compensated as required and the Fermi energy so obtained agrees with that fitted within our numerical accuracy (± 0.0005 a.u.), so that our calculation of the unstrained Fermi surface effectively involves only the two matrix elements as free parameters. The total bandwidth $E_{FB} = E_F - E_B$ (E_B refers to the bottom of the conduction band), increases with respect to the free-electron value due to the opening of a sizable gap between the first and the next three bands (smallest energy gap 4 OPW: 0.061 a.u., 8 OPW: 0.065 a.u., 16 OPW: 0.069 a.u.),

TABLE III. Equilibrium parameters for lead at 0 K.

Lattice constant (a.u.)[a]	$a = 9.2874$ (4.915 Å)
Volume per atom (a.u.)	$\Omega = 200.27$
Free-electron parameters (a.u.)	$E_F^0 = 0.352\,27$ $k_F^0 = 0.839\,37$
Elastic compliance constants[b] (10^{-6} bar^{-1})	$S_{11} = 6.8153$ $S_{12} = -3.0661$ $S_{44} = 5.1493$
Compressibility (10^{-6} bar^{-1})	$\kappa = 2.0495$

[a]The room-temperature lattice constant (Ref. 27) is converted to 0 K with thermal-expansion data (Ref. 28).

[b]Reference 29.

TABLE IV. Form factors at the first two reciprocal-lattice vectors, Fermi energies E_F, occupied bandwidth E_{FB}, and number of carriers per atom n_i in band i for different sizes of the secular matrix (energies in a.u.).

	4 OPW	8 OPW	16 OPW	AW[a]
v_{111}	−0.050 09	−0.046 77	−0.050 05	−0.046 78
v_{200}	−0.032 45	−0.026 51	−0.018 25	−0.019 93
E_F[b]	0.359 36	0.352 00	0.342 13	0.348 62
E_F[c]	0.3598	0.3518	0.3417	
E_{FB}[c]	0.3697	0.3695	0.3762	
E_{FB}[d]	0.3553	0.3576		
n_2(holes)[c]	−0.3750	−0.3676	−0.3675	
n_3(electrons)[c]	0.3715	0.3645	0.3674	
n_4(electrons)[c]	0.0034	0.0031	0.0000	

[a]Appapillai and Williams (Ref. 26).
[b]Fitted value.
[c]Calculated by summing over occupied states.
[d]Second-order perturbation theory, see Refs. 25 and 30.

an effect which overwhelms the expected contraction arising from the increased density of states at the Bragg planes.

For the $\zeta[110]$ orbits we have assumed that the higher and dominant frequency (see Fig. 5 and Table I) corresponds to the orbit centered at U,K in agreement with Van Dyke[5] and Anderson *et al.*[4] but in contrast to Anderson and Gold.[15] For *all* sizes of the secular matrix we find a second, smaller, noncentral orbit $\zeta_{nc}[110]$. Its exact position has been localized by extremalizing the area with the help of Eq. (3.7).

For the 4-OPW calculation the root-mean-square (rms) deviation for the eight fitted plus the $\zeta_{nc}[110]$ orbit is 2.0%. This is better than the result of Anderson *et al.*[4] for the local 4-OPW model (rms deviation 2.6% including ξ orbit). The same quantity for the 8-OPW case is 3.0% whereas for 16 OPW's it is 1.7%. Although the 4-CPW treatment apparently leads to a better fit than the 8-OPW calculation, one must keep in mind that the shape of the Fermi surface, particularly in the $(1\bar{1}0)$ plane through Γ, will show unphysical cusps due to our neglect of matrix elements, as important in size as the ones we have included. The best fit with an rms deviation of 0.45% was obtained by Van Dyke[5] with a local pseudopotential using about 90 OPW's, and Anderson *et al.*[4] using a nonlocal model achieved 1.5%. The better agreement is not surprising, because these authors include spin-orbit coupling and use three adjustable parameters, compared to our two in the local model. As the main objective of this work is to compare the predictions of various band-structure models for the strain response of the Fermi surface, we have not tried to improve the quality of our zero-pressure fit. This seems justified because it has been found that in other simple metals[8] the quality of the zero-pressure fit has relatively little influence on the values of the strain derivatives. Therefore we restrict ourselves to the minimum size of 8 OPW's, which is required for a correct treatment of shear deformations.[25] For this case the calculated areas together with their dependence on the fitting parameters are given in Table V. As the number of OPW's is varied, no systematic change is observed for the derivatives with respect to the matrix elements. The bare cyclotron masses $m_c = [1/(2\pi)](A/E_F)(\partial \ln A/\partial \ln E_F)$ remain nearly constant for most orbits when going from 4 to 16 OPW's. The results of our 8-OPW calculation are listed in Table VI together with experimentally determined cyclotron masses and the electron-phonon enhancement factor $\lambda = (m_c^{\text{expt}}/m_c^{\text{calc}})-1$. The latter is relatively constant for a given band, and its value in the second zone (0.82) is much smaller than in the third zone (1.40). A similar trend has been found by Anderson *et al.*[4] Both $\zeta[110]$ orbits have about the same enhancement if we use the recently published results of Ogawa and Aoki,[32] which confirms the assignment of the bigger area to the central orbit.

Our model predicts small electron pockets in the fourth zone at the point W (see Table V), whose extremal cross sections are between two and three times too small compared to those experimentally found by Ivowi and Mackinnon.[17] In the early calculations a special effort was made to suppress these fourth-zone pockets which had not yet been observed at the time. This was in fact one of the reasons why Anderson and Gold[15] introduced the spin-orbit coupling in their treatment. However with a better optimization[4] the fourth-zone pockets reappeared. In the nonlocal treatment of the pseudopotential by these authors

TABLE V. Experimental and calculated areas of some extremal orbits on the Fermi surface of lead and their dependence on the matrix elements and the Fermi energy in the 8-OPW case.

Orbit $[\vec{H}]$	Center $(2\pi/a)$	Area (a.u.) Expt.	Area (a.u.) Calc.	$\sum_{l\in G_s} \frac{\partial \ln A}{\partial \ln V_l}$ $\{\vec{G}_{111}\}$	$\sum_{l\in G_s} \frac{\partial \ln A}{\partial \ln V_l}$ $\{\vec{G}_{200}\}$	$\frac{\partial \ln A}{\partial \ln E_F}$
l[100]	$W(0,-1/2,1)$	0.0151[c]	0.00646	−14.65	4.068	73.5
l[110]	$W(0,-1/2,1)$	0.0118[c]	0.00409	−13.48	3.615	71.1
l[111]	$W(0,-1/2,1)$	0.0119[c]	0.00459	−13.48	3.643	70.8
ξ_c[110][a]	$U(1/4,-1/4,1)$	0.04831[d]	0.05019	−0.314	−0.271	9.63
ξ_{nc}[110]	$(0.39,-0.11,1)$	0.0472[b]	0.0453	−0.038	−0.521	11.76
ξ[111][a]	$U(1/4,-1/4,1)$	0.05980[e]	0.06030	−0.266	−0.304	9.79
ν[100][a]	$W(1/2,0,1)$	0.13698[d]	0.13454	0.266	−0.489	9.12
ω[110]	$W(1,0,1/2)$	0.107[c]	0.0971	−0.623	−0.329	13.24
ξ[100][a]	$X(1,0,0)$	0.0953[b]	0.0983	0.764	0.044	−7.73
θ[111][a]	$L(1/2,1/2,1/2)$	0.2919[b]	0.2964	−0.099	0.168	−3.98
ψ[100][a]	Γ	0.5463[f]	0.5666	−0.323	−0.106	−3.39
ψ[110][a]	Γ	0.4253[d,e,f]	0.4210	−0.229	−0.087	−3.15
ψ[111][a]	Γ	0.4136[b]	0.4001	−0.168	−0.131	−3.33

[a] Used in the least-squares fit for the optimum matrix elements and the Fermi energy.
[b] This work.
[c] Reference 17.
[d] Reference 19.
[e] Reference 4.
[f] Reference 18.

as well as in Van Dyke's calculation the fourth zone was empty again. The fourth-zone extremal orbits are much more sensitive to the choice of the matrix elements and the Fermi energy than all the other orbits, as displayed in Table V. It is therefore obvious that the correct dimension of these pockets can only result if the fourth-zone orbits are included in the fit for the optimum parameters. However, the data of Ivowi and Mackinnon makes it hard to assign frequency branches (Fig. 7). The [111] direction is the only direction of magnetic field, where symmetry considerations allow only one frequency for the fourth zone. The inclusion of the l[111] orbit in the fit to the nine extremal cross-sectional areas gives the following set of optimum parameters: $v_{111} = -0.0429$

TABLE VI. Experimental and calculated bare cyclotron masses and electron-phonon enhancement factor of some de Haas–van Alphen extremal orbits in lead. dHvA: de Haas–van Alphen effect. CR: cyclotron resonance.

Orbit $[\vec{H}]$	m_c^{expt} dHvA	m_c^{expt} CR	m_c^{calc}	$\lambda = (m_c^{expt}/m_c^{calc})-1$
ξ_c [110]	0.539 ±0.006[a]	0.537 ±0.001[d]	0.219	1.45
ξ_{nc}[110]	0.571 ±0.007[a]		0.241	1.37
ξ [111]	0.68 ±0.02[b]	0.69[e]	0.267	1.55
ν [100]	1.22 ±0.01[b]	1.22[e]	0.555	1.20
ω [110]		1.42[c,e]	0.581	1.44
ξ [100]	0.89 ±0.02[b]	0.93[e]	0.344	1.59
θ [111]	1.19 ±0.01[b]	1.20[e]	0.534	1.23
ψ [100]	1.51 ±0.03[b]	1.58[e]	0.869	0.74
ψ [110]	1.10 ±0.01[b]	1.120 ±0.002[d]	0.599	0.87
ψ [111]	1.12 ±0.01[b]	1.14[e]	0.603	0.86

[a] Reference 32.
[b] Reference 21.
[c] Reference 33.
[d] Reference 34.
[e] Reference 35.

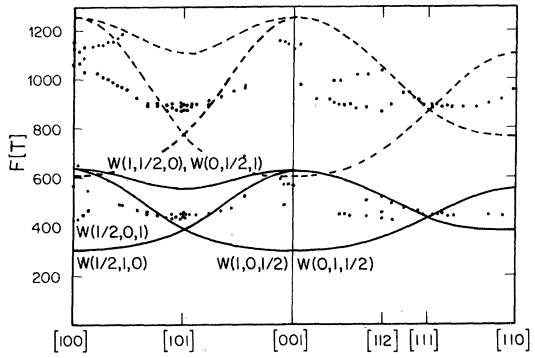

FIG. 7. Quantum oscillation frequencies ascribed to electron pockets in the fourth zone of lead as a function of field orientation, for magnetic fields in the (010) and (1$\bar{1}$0) planes. The data points were observed ultrasonically by Ivowi and Mackinnon (Ref. 17) and the solid curves show the predicted frequencies of our 8-OPW model; dashed curves: harmonic terms predicted from fundamental curves. The labels on the curves refer to the position of the relevant pocket in the Brillouin zone.

a.u., $v_{200}=0.0295$ a.u., $E_F=0.3530$ a.u.. The rms deviation for the nine areas increases to 5.3% and the different bands now contain the following number of carriers per atom: n_2 (holes) $=-0.3692$, n_3 (electrons) $=0.3592$, n_4 (electrons) $=0.0100$. The frequency branches predicted by this model are drawn in Fig. 7 together with the data points of Ivowi and Mackinnon. The agreement between theory and experiment is not particularly satisfactory, but the trends for, and the number of, frequency branches are correctly reproduced. We have deliberately left out from the figure the theoretical predictions of Ivowi and Mackinnon which are obviously wrong. Better experimental results for the fourth zone would present a really good test for the necessity and the magnitude of a spin-orbit parameter for the description of the unstrained Fermi surface of lead.

C. Strain dependence of the form factor and of the Fermi energy

The calculation of the homogeneous strain response of the Fermi surface requires the evaluation of the strain dependence of the Fermi energy and the matrix elements [Eq. (3.10)]. For the matrix elements we use the so-called "on-Fermi-sphere" approximation, which implies locality of the strain dependence of the form factor $v(|\vec{G}_i-\vec{G}_j|)$. For a monatomic Bravais lattice we can write $[v_s=v(|\vec{G}_s|)]$

$$\frac{dV_s}{d\epsilon}=\frac{dv_s}{d\epsilon}=\frac{\partial v}{\partial \ln q}\bigg|_{q=|\vec{G}_s|}\frac{d\ln|\vec{G}_s|}{d\epsilon}+\frac{\partial v_s}{\partial \ln k_F}\frac{d\ln k_F}{d\epsilon}\,, \tag{3.11}$$

where k_F is the radius of the free-electron sphere.

For volume-conserving shears γ is defined in Eqs. (2.3) and (2.4), k_F is constant, and the above equation reduces to

$$\frac{dv_s}{d\gamma}=\frac{\partial v}{\partial \ln q}\bigg|_{q=|\vec{G}_s|}\frac{d\ln|\vec{G}_s|}{d\gamma}\,. \tag{3.12}$$

For a pure volume change and for a cubic crystal it becomes

$$\frac{dv_s}{d\ln\Omega}=-\frac{1}{3}\left(\frac{\partial v}{\partial \ln q}\bigg|_{q=|\vec{G}_s|}+\frac{\partial v_s}{\partial \ln k_F}\right) \tag{3.13}$$

since both k_F and $|\vec{G}_s|$ are proportional to $\Omega^{-1/3}$. The partial derivatives of the form factor with respect to these arguments, computed at the first two reciprocal-lattice vectors, are given in Table VII. The slopes of the form factors $(\partial v/\partial \ln q)|_{q=|\vec{G}_{111}|}$ and $(\partial v/\partial \ln q)|_{q=|\vec{G}_{200}|}$, the *only* free parameters in our calculation of the strain response of the Fermi surface, result from a weighted least-squares fit to *all* presently available stress and pressure data listed in Table II. The partial derivatives $[\partial v(|\vec{G}_s|)/\partial \ln k_F]$ were calculated with the approximation[8] $v(q,k_F)=f(q)/$

TABLE VII. Comparison of the fitted form factor derivatives $\partial v/\partial \ln q$, $\partial v/\partial \ln k_F$, and $d\ln v/d\ln\Omega$ for different sizes of the secular matrix (in a.u.).

	$\vec{G}_s$	4 OPW	8 OPW	16 OPW	AW[a]
$(\partial v/\partial \ln q)\|_{q=\|\vec{G}_s\|}$	$\vec{G}_{111}$	0.190 ±0.020	0.167 ±0.015	0.129 ±0.026	0.180
	$\vec{G}_{200}$	0.173 ±0.011	0.146 ±0.007	0.131 ±0.014	0.198
$\partial v(\|\vec{G}_s\|)/\partial \ln k_F$	$\vec{G}_{111}$	−0.1208	−0.1128	−0.1207	−0.1128
	$\vec{G}_{200}$	−0.0791	−0.0646	−0.0445	−0.0486
$d\ln v(\|\vec{G}_s\|)/d\ln\Omega$	$\vec{G}_{111}$	0.458	0.386	0.052	0.476
	$\vec{G}_{200}$	0.966	1.028	1.589	2.495

[a] Appapillai and Williams (Ref. 26).

$[\Omega\epsilon(q,k_F)]$, where $\epsilon(q,k_F)$ is the Hartree dielectric function. The corresponding quantities at higher wave vector were set to zero, which is consistent with our treatment of the unstrained Fermi surface. Increasing the number of OPW's from 8 to 16 brings no improvement to the quality of the fit, and the slopes at the first two reciprocal-lattice vectors are not very different from those of the Appapillai and Williams[26] form factor, but they do not tend towards the latter as the size of the secular matrix is increased. In view of the fact that our fitting procedure places no constraints on the derivatives of the form factor $\partial v/\partial \ln q$, the agreement with Appapillai and Williams is satisfactory. Similar results have been obtained for other simple metals, such as aluminum,[25] indium, zinc, and magnesium.[8]

The Fermi energy only depends on the strain through the accompanying volume change, and the volume dependence is given by

$$\frac{d\ln E_F}{d\ln\Omega} = \frac{\partial \ln E_F}{\partial \ln\Omega}\bigg|_{V_s} + \sum_s \frac{\partial \ln E_F}{\partial V_s}\,\frac{dV_s}{d\ln\Omega}\,. \tag{3.14}$$

The different partial derivatives of the Fermi energy appearing in the volume dependence of the latter are listed in Table VIII. They are computed by using the Hellman-Feyman theorem and summing over occupied states.[25] The total volume dependence of the width of the occupied part of the conduction band is compared with the value found by second-order perturbation theory. In the latter approach the change of the bottom of the band with volume is included, and is in fact by far the dominant contribution.

D. Shear dependence of the Fermi surface

Shears, tetragonal or angular, are volume conserving by definition so that their effect on extremal areas reduces to

$$\frac{d\ln A}{d\gamma} = \frac{\partial \ln A}{\partial \gamma}\bigg|_{V_s} + \sum_s \frac{\partial \ln A}{\partial V_s}\,\frac{dV_s}{d\gamma}\,, \tag{3.15}$$

where the first term on the right-hand side accounts for the change in geometry associated with the shear γ. The dependence of the matrix elements on γ is given in Eq. (3.12). Note that for a tetragonal shear $d\ln|\vec{G}_{111}|/d\gamma_i$ vanishes, and the only parameter entering our 8-OPW calculation of the shear dependence is the derivative of the form factor at $q=|\vec{G}_{200}|$. The different contributions to the tetragonal shear dependence of some extremal orbits are presented in Table IX. They were calculated with $(\partial v/\partial \ln q)|_{q=|\vec{G}_{200}|}$ resulting from the fit to *all* presently available pressure and stress data. The final results agree within error bars with the experimental data deduced from the measured uniaxial stress dependence by means of relation (2.13). The value of the form-factor derivative determined to give the best fit to the experimental tetragonal shear data is

$$\frac{\partial v}{\partial \ln q}\bigg|_{q=|\vec{G}_{200}|} = 0.179 \text{ a.u.}$$

and is now in fair agreement with the Appapillai and Williams[26] form-factor derivative of 0.198 a.u. at $q=|\vec{G}_{200}|$. For each orbit the three derivatives with respect to γ_x, γ_y, and γ_z have been computed independently, and in all cases the $\partial \ln A/\partial\gamma_i$ and $d\ln A/d\gamma_i$ add up to zero as they should. Except for the $\zeta_{n_c}[110]$, $\nu[100]$, and

TABLE VIII. Partial derivatives of the Fermi energy with respect to the atomic volume Ω and the matrix elements V_s for different sizes of the secular matrix. The total derivatives of the Fermi energy and the occupied bandwidth are computed with the slopes of the form factor given in Table VII (in a.u.).

	G_s	4 OPW	8 OPW	16 OPW
$\partial\ln E_F/\partial\ln\Omega$		−0.641	−0.664	−0.704
$\sum_{l\in G_s} \partial\ln E_F/\partial V_l$	$\{\vec{G}_{111}\}$	−0.461	0.141	1.308
	$\{\vec{G}_{200}\}$	−0.543	−0.417	−0.490
$d\ln E_F/d\ln\Omega$		−0.613	−0.655	−0.693
$d\ln E_{FB}/d\ln\Omega$		−0.596	−0.624	−0.631
$d\ln E_{FB}/d\ln\Omega$[a]		−0.653	−0.645	

[a] Second-order perturbation theory, see Refs. 25 and 30.

TABLE IX. Experimental and theoretical tetragonal shear dependence of the area of some extremal orbits on the Fermi surface of lead. The theoretical values are calculated in the 8-OPW case with $(\partial v/\partial \ln q)|_{q=|\vec{G}_s|}$ given in Table VII, column 4 (fitted values). For the centers of the orbits see Table V.

Orbit $[\vec{H}]$	i	$\frac{\partial \ln A}{\partial \gamma_i}$	$\frac{\partial \ln A}{\partial V_{200}}\frac{dV_{200}}{d\gamma_i}$	$\frac{\partial \ln A}{\partial V_{020}}\frac{dV_{020}}{d\gamma_i}$	$\frac{\partial \ln A}{\partial V_{002}}\frac{dV_{002}}{d\gamma_i}$	$\frac{d\ln A}{d\gamma_i}$ Calc.	$\frac{d\ln A}{d\gamma_i}$ Expt.
ζ_c[110]	x	−3.045	−0.314	0.157	0.436	−2.77	−2.53 ± 0.40
	y	−3.045	0.157	−0.314	0.436	−2.77	−2.53 ± 0.40
	z	6.089	0.157	0.157	−0.871	5.53	5.06 ± 0.81
ζ_{nc}[110]	x	−3.867	−0.103	0.757	0.629	−2.58	
	y	−0.318	0.052	−1.514	0.629	−1.15	
	z	4.185	0.052	0.757	−1.259	3.73	
ζ[111]	x	−2.882	−0.376	0.188	0.463	−2.61	
	y	−2.882	0.188	−0.376	0.463	−2.61	
	z	5.765	0.188	0.188	−0.925	5.22	
ν[100]	x	−3.257	−0.005	0.674	0.674	−1.92	−1.72 ± 0.30
	y	1.629	0.003	−1.348	0.674	0.96	0.86 ± 0.15
	z	1.629	0.003	0.674	−1.348	0.96	0.86 ± 0.15
ω[110]	x	2.050	−0.724	0.362	0.183	1.87	
	y	2.050	0.362	−0.724	0.183	1.87	
	z	−4.100	0.362	0.362	−0.366	−3.74	
ξ[100]	x	5.340	−0.615	−0.215	−0.215	4.30	4.15 ± 0.30
	y	−2.670	0.307	0.430	−0.215	−2.15	−2.07 ± 0.15
	z	−2.670	0.307	−0.215	0.430	−2.15	−2.07 ± 0.15
ψ[100]	x	0.517	−0.845	−0.065	−0.065	−0.46	
	y	−0.259	0.423	0.131	−0.065	0.23	
	z	−0.259	0.423	−0.065	0.131	0.23	
ψ[110]	x	0.573	−0.218	0.109	0.022	0.49	0.48 ± 0.03
	y	0.573	0.109	−0.218	0.022	0.49	0.48 ± 0.03
	z	−1.147	0.109	0.109	−0.044	−0.97	−0.96 ± 0.06

ψ[100] orbit, the dominant contribution to $d\ln A/d\gamma_i$ is seen to arise from the pure change in geometry induced by the shear. For the orbits θ[111] and ψ[111] we find $(d\ln A/d\gamma_i)_{i=x,y,z}=0$, as expected from symmetry considerations. The influence of a tetragonal shear on the shape of the Fermi surface of lead in different planes is illustrated in Fig. 8.

For angular shear $d\ln|\vec{G}_{200}|/d\gamma_{ij}$ vanishes so that the only dependence is on the form factor at $q=|\vec{G}_{111}|$. The different contributions to the shear dependence in Table X are calculated with the fitted value of $(\partial v/\partial \ln q)|_{q=\vec{G}_{111}}$ quoted in Table VII. The two experimental values listed were obtained with the help of Eq. (2.8) from two different measurements of the uniaxial stress dependence with stress parallel to the [100] and [110] crystallographic direction. The agreement between the calculated and measured angular shear dependence is remarkable, given the size of the experimental errors. The influence of angular shears on the shape of the Fermi surface of lead in a $(1\bar{1}0)$ and (001) plane is illustrated in Fig. 9.

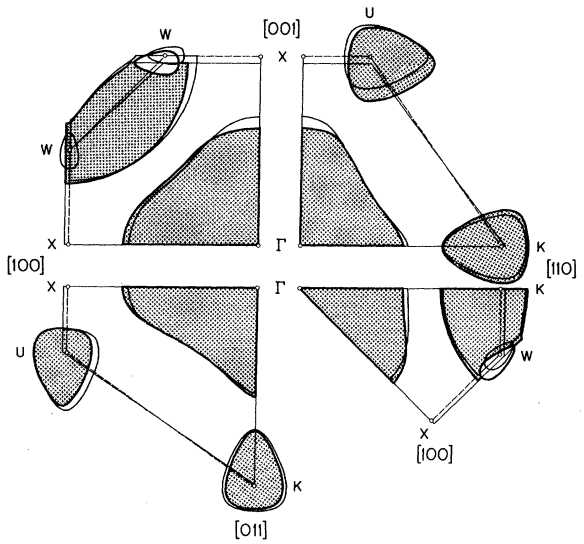

FIG. 8. Response of the Fermi surface of lead to a tetragonal shear $\gamma_z=0.04$. The unstrained Brillouin zone is dashed and the deformed orbits are shadowed.

TABLE X. Experimental and theoretical angular shear dependence of the area of some extremal orbits on the Fermi surface of lead. The theoretical values are calculated in the 8-OPW case with $(\partial v/\partial \ln q)|_{q=|\vec{G}_s|}$ given in Table VII, column 4 (fitted values). γ_{ij} is measured in radians. For the centers of the orbits see Table V.

Orbit $[\vec{H}]$	ij	$\frac{\partial \ln A}{\partial \gamma_{ij}}$	$\sum_{l\in G_s} \frac{\partial \ln A}{\partial V_l}\frac{dV_l}{d\gamma_{ij}}$		$\frac{d\ln A}{d\gamma_{ij}}$	
			$\left.\begin{matrix}\vec{G}_{111},\vec{G}_{\bar{1}\bar{1}\bar{1}}\\ \vec{G}_{11\bar{1}},\vec{G}_{\bar{1}\bar{1}1}\end{matrix}\right\}\in G_s$	$\left.\begin{matrix}\vec{G}_{1\bar{1}1},\vec{G}_{\bar{1}1\bar{1}}\\ \vec{G}_{\bar{1}11},G_{1\bar{1}\bar{1}}\end{matrix}\right\}\in G_s$	Calc.	Expt.
ζ_c[110]	xy	−2.559	0.574	0.948	−1.04	−0.78 ± 3.11
	yz, zx				0.00	
ζ_{nc}[110]	xy	−1.622	0.912	0.958	0.25	
	yz, zx				0.00	
ζ[111]	xy	−2.429	0.627	0.943	−0.86	
	yz, zx				0.00	
ν[100]	xy, yz, zx				0.00	
ω[110]	xy	−0.284	0.582	1.324	1.62	
	yz, zx				0.00	
ξ[100]	xy, yz, zx				0.00	
θ[111]	xy, yz, zx	1.200	−0.089[a]	0.028[a]	1.14	
ψ[100]	xy, yz, zx				0.00	
ψ[110]	xy	1.887	−0.270	0.002	1.62	1.59 ± 0.19
	yz, zx				0.00	
ψ[111]	xy, yz, zx	0.696	−0.219[a]	−0.020[a]	0.46	

[a] Values listed for γ_{xy}.

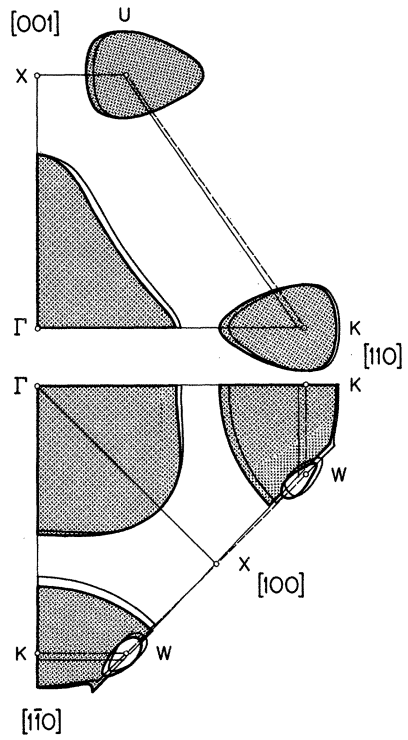

FIG. 9. Angular shear dependence of the Fermi surface of lead in the (1$\bar{1}$0) and (001) planes. The unstrained Brillouin zone is dashed and the shadowed orbits correspond to an angular shear $\gamma_{xy}=3°$.

E. Volume dependence of the Fermi surface

The dependence of extremal areas on dilation is given by

$$\frac{d\ln A}{d\ln\Omega} = -\frac{2}{3} + \sum_s \frac{\partial \ln A}{\partial \ln V_s}\left(\frac{2}{3} + \frac{d\ln V_s}{d\ln\Omega}\right) + \frac{\partial \ln A}{\partial \ln E_F}\left(\frac{2}{3} + \frac{d\ln E_F}{d\ln\Omega}\right), \tag{3.16}$$

which follows from Eq. (3.10) and the exact expression

$$\left.\frac{\partial \ln A}{\partial \ln\Omega}\right|_{E_F,V_s} = -\frac{2}{3}\left(1 - \frac{\partial \ln A}{\partial \ln E_F} - \sum_s \frac{\partial \ln A}{\partial \ln V_s}\right), \tag{3.17}$$

which is best derived from Sorbello and Griessen's[6] scaling relation for A. Equation (3.17) couples all partial derivatives of A used for the description of the strain response of the Fermi surface and provides us with a nice consistency check. In all cases this relation was satisfied to better than 1 part in 10^6. The first term on the right-hand side of Eq. (3.16) is the free-electron result, the

other two are the deviations from it, and the different contributions for some extremal areas are summarized in Table XI. They were calculated from the volume derivatives of V_{111}, V_{200}, and E_F using the slopes of the form factor at the first reciprocal-lattice vectors obtained from the fit to *all* presently available experimental pressure and stress data. The final results are compared to the dilation response calculated from the hydrostatic pressure values of Anderson *et al.*[4] using Eq. (2.12). Except for the $\zeta_c[110]$ and $\psi[110]$ orbits the experimental and calculated dilation dependences agree within errors. This is significantly better than the results of all the previous model calculations (Fig. 10), except those of Anderson *et al.*,[4] who used a nonlocal pseudopotential with a core radius dependent on the lattice parameter, and spin-orbit interaction. With these partly unphysical refinements they reached an absolute rms deviation between theory and experiment of 0.11, which is only slightly better than our value of 0.14 obtained with a model for the strain response which not only explains pressure but also uniaxial stress data with the same set of two parameters. The influence of dilation on the shape of the Fermi surface of lead in the (010) and $(1\bar{1}0)$ planes, calculated with our fitted values, is illustrated in Fig. 11. The interested reader may consult Table 7.2 of Fawcett *et al.*[7] for a summary of the theoretical predictions for the dilation dependence which have appeared in the literature. We do not understand why the local pseudopotential calculation of Anderson *et al.*[4] failed to reproduce the experimental results. It is also not clear to us why Van Dyke's[5] calculation produces such an exaggerated pressure dependence of the $\xi[100]$ and $\psi[100]$ orbits. Anderson *et al.*[3,36] neglect the change in lattice constant with pressure in their form-factor derivatives so that, compared to our Eq. (3.16), their expression omits the term $\frac{2}{3}(\sum_s \partial \ln A/\partial \ln V_s)$. Furthermore they assume a free-electron behavior for the Fermi energy. Whereas the latter assumption at most produces a ten percent contribution to the dilation dependence (Table XI), the importance of the omitted term is obvious from Table V, where its value is seen to vary between +0.54 for the $\xi[100]$ orbit and −0.63 for the $\omega[110]$ orbit. It is this term which is responsible for the deviation from free-electron behavior and not the fact that the pseudopotential model has not reached convergence due to the use of a small number of plane waves as asserted by Van Dyke. This has been explicitly tested by repeating our calculation for 4 and 16 OPW's.

IV. CONCLUSIONS

We have presented in this paper a detailed investigation of the effect of a homogeneous strain on the Fermi surface of lead. The combined oscillatory magnetostriction and de Haas–van Alphen torque method was used to measure the uniaxial stress dependence of extremal cross sections of the Fermi surface. For the first time the method was also applied to obtain angular shear dependences and has proved to be effective. From our complete uniaxial stress data we have determined the tetragonal shear and dilation dependence of the area of several extremal orbits in high-symmetry planes on the Fermi surface. Our results for the dilation dependence are in good agreement with the values of Anderson *et al.*,[4] which were obtained directly using hydrostatic pressure.

TABLE XI. Experimental and theoretical volume dependence of the area of some extremal orbits on the Fermi surface of lead. The theoretical values are calculated in the 8-OPW case with $d\ln w_s/d\ln\Omega$ given in Table VII, column 4 (fitted values) and $d\ln E_F/d\ln\Omega$ given in Table VIII, column 4. For the orbit centers see Table V.

Orbit $[\vec{H}]$	$\sum_{l\in G_s} \frac{\partial \ln A}{\partial \ln V_l}\left(\frac{2}{3}+\frac{d\ln V_l}{d\ln\Omega}\right)$ $G_s\in\{\vec{G}_{111}\}$	$G_s\in\{\vec{G}_{200}\}$	$\frac{\partial \ln A}{\partial \ln E_F}\left(\frac{2}{3}+\frac{d\ln E_F}{d\ln\Omega}\right)$	$\frac{d\ln A}{d\ln\Omega}$ Calc.	Expt.[a]
$\zeta_c[110]$	−0.331	−0.460	0.114	−1.34	−1.22 ± 0.10
$\zeta_{nc}[110]$	−0.040	−0.883	0.139	−1.45	
$\zeta[111]$	−0.280	−0.515	0.116	−1.35	−1.32 ± 0.10
$\nu[100]$	0.238	−0.829	0.108	−1.15	−1.12 ± 0.05
$\omega[110]$	−0.656	−0.557	0.157	−1.72	
$\xi[100]$	0.805	0.075	−0.091	0.12	0.00 ± 0.15
$\theta[111]$	−0.104	0.285	−0.047	−0.53	−0.59 ± 0.05
$\psi[100]$	−0.340	−0.179	−0.040	−1.23	−1.17 ± 0.20
$\psi[110]$	−0.241	−0.147	−0.037	−1.09	−1.41 ± 0.10
$\psi[111]$	−0.177	−0.221	−0.039	−1.10	−1.02 ± 0.10

[a] Experimental values, Ref. 4.

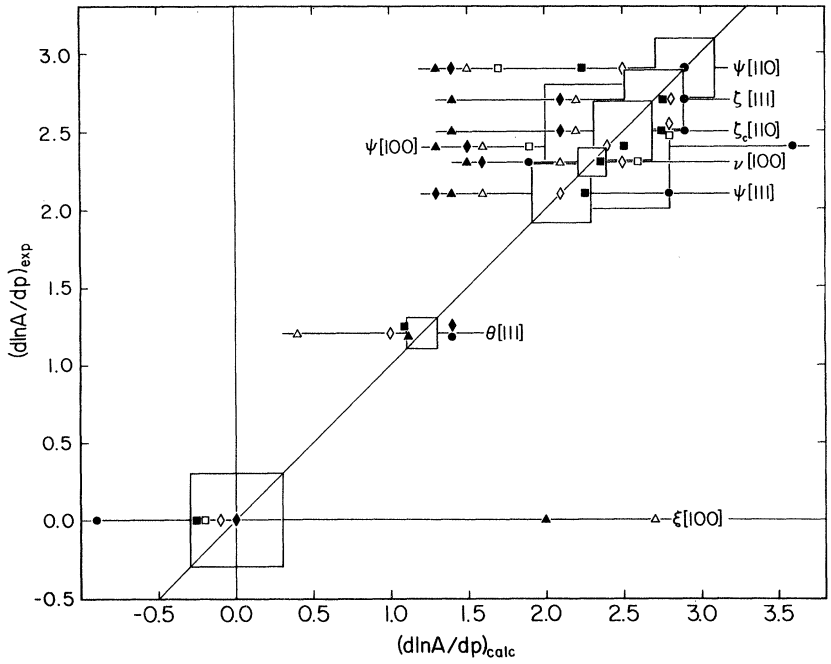

FIG. 10. Experimental hydrostatic pressure dependence (Ref. 4) plotted against values calculated by different authors for several extremal orbits of the Fermi surface of lead. Agreement within experimental error bars is given for points lying inside the square of the corresponding orbit. ■ this work; ▲, △, ♦, ◇ Anderson *et al.* (Ref. 4): 4-OPW pseudopotential calculation including spin–orbit interaction, ▲ local potential, △ local volume-dependent potential, ♦ nonlocal potential, ◇ nonlocal volume-dependent potential; ● Van Dyke (Ref. 5): 90-OPW pseudopotential calculation including spin–orbit interaction; □ Sorbello and Griessen (Ref. 6): 4-OPW calculation with local pseudopotential.

We have shown that a local pseudopotential model, without invoking spin-orbit interaction and using a small number of OPW's, can explain all the experimental data. The description of a general homogeneous strain requires the inclusion of eight reciprocal-lattice vectors in the secular matrix and a further increase in the size of the latter brings no improvement in our results. The Fermi energy and its derivatives are computed by summing over occupied states. The small deviation of the volume dependence of the Fermi energy from the free-electron behavior is relatively unimportant for the response of extremal orbits on the Fermi surface to a uniform dilation. Our fit to the experimental dilation dependence involves only two free parameters, namely the slope of the form factor at the first two reciprocal-lattice vectors ($q = |\vec{G}_{111}|, |\vec{G}_{200}|$). From the tetragonal shear data we gain information about the slope of the form factor at $q = |\vec{G}_{200}|$, whereas the angular shear experiment is complementary and gives us access to the slope of the form factor at $q = |\vec{G}_{111}|$.

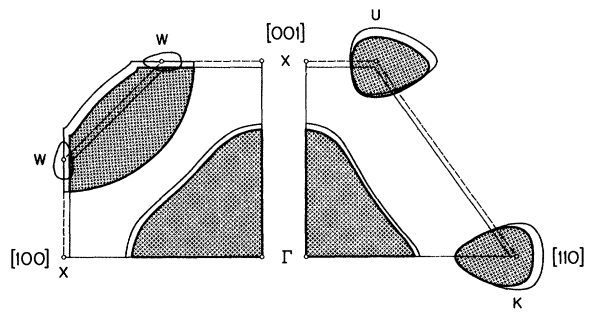

FIG. 11. Deformation of the Fermi surface of lead in a (010) and (1$\bar{1}$0) plane, corresponding to a dilation $\Delta\Omega/\Omega = 0.10$. The unstrained Brillouin zone is dashed and the deformed orbits are shadowed.

ACKNOWLEDGMENTS

I wish to express my gratitude to Professor J. L. Olsen for his support, continued interest, and kind encouragement throughout the course of this work. I am very grateful to Professor R. Griessen and Dr. R. Monnier for their interest and for many helpful and stimulating discussions about the theoretical aspects of this work, and further I thank Dr. W. van der Mark for many ideas concerning the experimental techniques and the minicomputer-based data-acquisition system. I would also like to thank Dr. M. Posternak for the advice on the band-structure calculation in the early stages of this work, and A. Vogelsanger and

W. Schmid for the high-precision machining of the dilatorquemeters. For the skillful preparation of the lead samples I am indebted to P. Caminada. I am very grateful to Dr. R. Monnier for all the helpful comments during the preparation of the manuscript. This work has benefited from the financial support of the Schweizerischer Nationalfonds zur Förderung der wissenschaftlichen Forschung.

[1]V. Heine, in *Solid State Physics,* edited by H. Ehrenreich, F. Seitz, and D. Turnbull (Academic, New York, 1970), Vol. 24, pp. 1–36.
[2]M. L. Cohen and V. Heine, in *Solid State Physics,* edited by H. Ehrenreich, F. Seitz, and D. Turnbull (Academic, New York, 1970), Vol. 24, pp. 37–248.
[3]J. R. Anderson, W. J. O'Sullivan, and J. E. Schirber, Phys. Rev. 153, 721 (1967).
[4]J. R. Anderson, W. J. O'Sullivan, and J. E. Schirber, Phys. Rev. B 5, 4683 (1972).
[5]J. P. Van Dyke, Phys. Rev. B 7, 2358 (1973).
[6]R. S. Sorbello and R. Griessen, Solid State Commun. 12, 689 (1973).
[7]E. Fawcett, R. Griessen, W. Joss, M. J. G. Lee, and J. M. Perz, in *Electrons at the Fermi Surface,* edited by M. Springford (Cambridge University Press, Cambridge, 1980), pp. 278–318.
[8]R. Griessen and R. S. Sorbello, J. Low Temp. Phys. 16, 237 (1974).
[9]I. M. Lifshitz and A. M. Kosevich, Zh. Eskp. Teor. Fiz. 29, 730 (1955) [Sov. Phys.–JETP 2, 636 (1956)].
[10]G. Brändli and R. Griessen, Cryogenics 13, 299 (1973).
[11]R. Griessen, M. J. G. Lee, and D. J. Stanley, Phys. Rev. B 16, 4385 (1977).
[12]Berylco 25, from Kawecki Berylco Industries, Inc., New York.
[13]L. R. Rabiner and B. Gold, *Theory and Application of Digital Signal Processing* (Prentice Hall, Englewood Cliffs, New Jersey, 1975) pp. 75–204.
[14]J. Lang and R. Müller, Comput. Phys. Commun. 2, 79 (1971).
[15]J. R. Anderson and A. V. Gold, Phys. Rev. 139, A1459 (1965).
[16]P. J. Tobin, D. J. Sellmyer, and B. L. Averbach, Phys. Lett. 28A, 723 (1969).
[17]U. M. O. Ivowi and L. Mackinnon, J. Phys. F 6, 329 (1976).
[18]J. R. Anderson and D. C. Hines, Phys. Rev. B 2, 4752 (1970).
[19]J. R. Anderson, J. Y. M. Lee, and D. R. Stone, Phys. Rev. B 11, 1308 (1975).
[20]A. V. Gold and P. W. Schmor, Can. J. Phys. 54, 2445 (1976).
[21]R. A. Phillips and A. V. Gold, Phys. Rev. 178, 932 (1969).
[22]W. Joss and W. van der Mark, J. Phys. (Paris) Colloq. 39, C6-1093 (1978).
[23]P. O. Löwdin, J. Mol. Spectrosc. 13, 326 (1964).
[24]J. C. Shaw, J. B. Ketterson, and L. R. Windmiller, Phys. Rev. B 5, 3894 (1972).
[25]W. Joss and R. Monnier, J. Phys. F 10, 9 (1980).
[26]M. Appapillai and A. R. Williams, J. Phys. F 3, 759 (1973).
[27]W. B. Pearson, *Handbook of Lattice Spacings and Structures of Metals and Alloys* (Pergamon, Oxford, 1958).
[28]Y. S. Touloukian, R. K. Kirby, R. E. Taylor, and P. D. Desai, in *Thermal Expansion-Metallic Elements and Alloys, Thermophysical Properties of Matter,* edited by Y. S. Touloukian (IFI/Plenum, New York, 1975), Vol. 12, pp. 179–185.
[29]D. L. Waldorf and G. A. Alers, J. Appl. Phys. 33, 3266 (1962).
[30]W. A. Harrison, *Pseudopotentials in the Theory of Metals* (Benjamin, New York, 1966), p. 96.
[31]G. Gilat and L. J. Raubenheimer, Phys. Rev. 144, 390 (1966).
[32]K. Ogawa and H. Aoki, J. Phys. F 8, 1169 (1978).
[33]Y. Onuki, H. Suematsu, and S. I. Tanuma, J. Phys. Chem. Solids 38, 419 (1977); 38, 431 (1977).
[34]I. Ya. Krasnopolin and M. S. Khaikin, Zh. Eksp. Teor. Fiz. 64, 1750 (1973) [Sov. Phys.–JETP 37, 883 (1973)].
[35]M. S. Khaikin and R. T. Mina, Zh. Eksp. Teor. Fiz. 42, 35 (1962) [Sov. Phys.–JETP 15, 24 (1962)]; R. T. Mina and M. S. Khaikin, Zh. Eksp. Teor. Fiz. 45, 1304 (1963) [Sov. Phys.–JETP 18, 896 (1964)].
[36]W. J. O'Sullivan, J. E. Schirber, and J. R. Anderson, Solid State Commun. 5, 525 (1967).

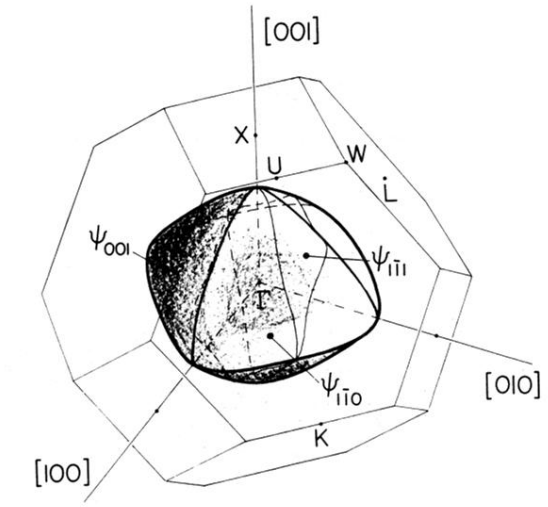

FIG. 2. Second-zone hole sheet of the Fermi surface of lead. The orbit ψ is drawn for the magnetic fields in the [001], [1$\bar{1}$0], and [1$\bar{1}$1] direction.

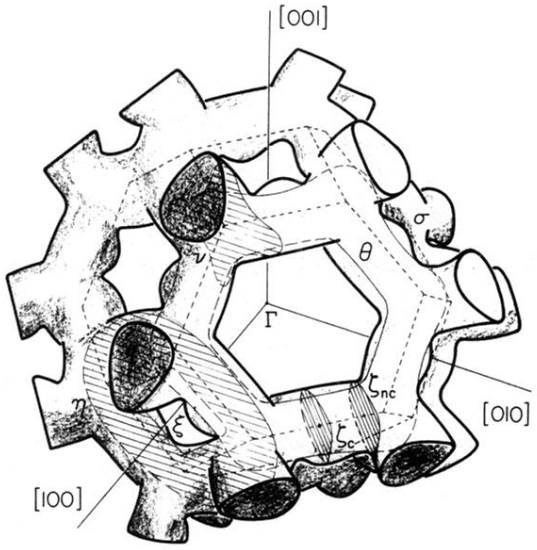

FIG. 3. Third-zone electron sheet of the Fermi surface of lead. The orbits ν, ξ, and η are drawn for the magnetic field in the [100] direction, ζ in the $[1\bar{1}0]$ direction, and θ and σ in the [111] direction.